Dalton Transactions

PAPER

Check for updates

Polypyridyl ruthenium(II) complexes functionalized with fatty acids for photodynamic therapy and induction of pyroptosis

Yuan Xu,[a,b] Yatao Hu,[a] Jiaping Cao,[a] Dixin Lin,[a] Qiqi Zhong,[a] Yi Wang,*[a] Hongdong Shi*[c] and Qianling Zhang (ID) *[a]

To address the challenges associated with the low cellular uptake efficiency of metal-based anticancer agents and the suboptimal therapeutic efficacy of photodynamic therapy (PDT), a series of polypyridyl ruthenium(II) complexes (Ru–Cn) with tunable carbon chain lengths were rationally designed and synthesized through the incorporation of fatty acid moieties, which confer enhanced lipid solubility and membrane-targeting capabilities. Among these, the octadecanoic acid-modified ruthenium complex (Ru-C18) exhibited superior anticancer activity. Cytotoxicity assays demonstrated that Ru-C18 displayed sub-molar cytotoxic potency under light irradiation. Co-localization studies confirmed its preferential accumulation in lysosomes after cellular internalization. Upon light activation, Ru-C18 efficiently generated singlet oxygen and induced hallmark features of pyroptosis, including plasma membrane blebbing, cellular swelling, and gasdermin-dependent membrane pore formation. Consequently, Ru-C18 significantly suppressed tumor cell proliferation *via* activation of the pyroptotic pathway. These findings offer new insights into the rational design of highly effective and selectively targeted photodynamic anticancer agents.

Introduction

According to the International Agency for Research on Cancer's GLOBOCAN 2022 report, cancer remains a leading global cause of morbidity and mortality, underscoring the urgent need for the development of novel therapeutic agents.[1,2] Platinum-based drugs (*e.g.*, cisplatin[3–5] and oxaliplatin[6–8]) constitute the foundation of approximately 50% of the current chemotherapeutic regimens and are included in 80% of the combination therapies.[9,10] However, their clinical application is substantially limited by severe adverse effects, including nephrotoxicity, nausea, and myelosuppression.[11–13] Moreover, certain tumors exhibit intrinsic resistance to platinum-based agents, which collectively impair therapeutic outcomes.[14,15]

Ruthenium complexes, owing to their distinctive chemical properties and favorable biological profiles, exhibit a wider

*aShenzhen Key Lab of Functional Polymer, College of Chemistry and Environmental Engineering, Shenzhen University, Shenzhen 518060, P. R. China.
E-mail: zhql@szu.edu.cn*
bCollege of Physics and Optoelectronic Engineering, Shenzhen University, Shenzhen, 518060, P.R. China
*cYunnan Key Laboratory of Stem Cell and Regenerative Medicine, College of Rehabilitation, Kunming Medical University, Kunming, 650500, P. R. China.
E-mail: shihongdong@kmmu.edu.cn*

therapeutic window and reduced toxicity compared to platinum-based chemotherapeutic agents.[16–19] These complexes selectively target cancer cells to induce apoptosis, inhibit proliferation, and modulate the tumor microenvironment, including the enhancement of immune responses through macrophage inhibition or activation of immune cells.[20,21] Critically, these agents disrupt tumor bioenergetics through concurrent targeting of mitochondrial function and oncogenic signaling pathways, thereby enhancing the efficacy of chemotherapy and demonstrating significantly improved therapeutic outcomes against drug-resistant malignancies when compared to conventional platinum-based agents.[22–25]

Ruthenium(II) complexes utilize their octahedral coordination geometry to function as highly promising photosensitizers in photodynamic therapy (PDT) for anticancer applications.[26–29] Upon light irradiation, these complexes generate reactive oxygen species (ROS), inducing cancer cell death *via* apoptosis, necrosis, or pyroptosis.[30–33] The structural versatility of these complexes allows for precise modulation through ligand engineering, thereby improving key properties including photosensitivity, tumor selectivity, and biocompatibility.

Notably, certain metal complexes have been demonstrated to induce gasdermin-mediated pyroptosis, a form of programmed inflammatory cell death.[34,35] For instance, the

rhenium(I) complex CAIX-Re represents the first light-activated pyroptosis inducer, and triggers antitumor immune responses *via* pyroptotic mechanisms upon light irradiation.[36]

Subsequent studies have further demonstrated the capacity of iridium(III), platinum(II), and related metal complexes to photodynamically induce pyroptosis.[37–40] A tetrazine-conjugated ruthenium(II) complex facilitates ultrasound-triggered and tumor-selective pyroptosis through a bioorthogonal cell membrane anchoring strategy.[41,42]

In targeted cancer therapy employing metal complexes, ligand design plays a pivotal role in modulating biological activity. The functionalization of pyridine ligands can substantially enhance the targeting specificity and therapeutic efficacy of polypyridyl ruthenium(II) complexes.[43] As the fundamental structural component of biomembrane systems, the phospholipid bilayer allows lipids to maintain membrane homeostasis while creating specialized microenvironments essential for biochemical reactions. Disruption of tumor cell membranes to induce intracellular content leakage constitutes a promising antitumor strategy. Saturated fatty acids with varying carbon chain lengths demonstrate distinct biological activities: short-chain fatty acids, such as butyric acid (C4), induce tumor cell apoptosis through epigenetic regulatory mechanisms; medium-chain fatty acids, including octanoic acid (C8) and lauric acid (C12), exert antitumor and antibacterial effects by destabilizing pathogenic lipid membrane structures; and long-chain fatty acids, such as stearic acid (C18), modulate cholesterol metabolism and aid in the elimination of toxic metal ions.[44–46]

Leveraging these properties, a library of amphiphilic photosensitizers was constructed by conjugating saturated fatty acids of varying chain lengths to polypyridyl ruthenium(II) complexes (Ru–Cn) (Scheme 1). The experimental results demonstrate that the cellular uptake of Ru–Cn compounds increases significantly with the elongation of the carbon chain, concomitant with a substantial enhancement in cytotoxicity. Notably, Ru-C18 displayed the highest antitumor potency, with a half-maximal inhibitory concentration (IC$_{50}$) in the submicromolar range (IC$_{50} \approx 0.3$ μM). Notably, upon irradiation at 465 nm, Ru-C18 efficiently generates singlet oxygen, which activates the caspase-1/GSDMD-mediated pyroptosis pathway, characterized by cell swelling and membrane rupture. This ultimately results in extensive tumor cell death. The strategy leverages the biocompatibility and membrane-targeting properties of fatty acids, enabling effective and low-toxicity PDT for cancer treatment, while also offering mechanistic insights into the efficient induction of tumor cell death.

Results and discussion

The synthesis route of the Ru(phen)$_2$Cl$_2$(phen-NH$_2$)-fatty acid (Ru–Cn) complex is illustrated in Fig. S1. The Ru(II) complexes with varying carbon chain lengths were synthesized and characterized through ^{1}H NMR and mass spectrometry (MS) analyses, as detailed in the Experimental section and the SI (Fig. S2–S12).

The UV-vis absorption spectra are presented in Fig. 1A. All six Ru(II) complexes exhibited absorption below 325 nm, which can be attributed to the intrinsic vibrations of benzene rings and π → π* transitions within the conjugated double-bond systems. This spectral region corresponds to B-band absorption. These features are closely related to the electronic structure of aromatic rings in organic molecules, indicating that the ligands in the Ru(II) complexes maintain their characteristic aromatic nature. Notably, within the wavelength range of 325 nm to 530 nm, the Ru(II) complexes exhibited strong absorption, with a well-defined absorption maximum at 448 nm. These complexes also demonstrated prominent photophysical and photochemical properties arising from metal-to-ligand charge transfer (MLCT), wherein d-electrons from the ruthenium(II) center are transferred to the π* orbitals of the ligands, thereby facilitating efficient ROS generation upon light irradiation.

Although all complexes exhibit emission at 597 nm (Fig. 1B), Ru-C18 demonstrates significantly enhanced fluo-
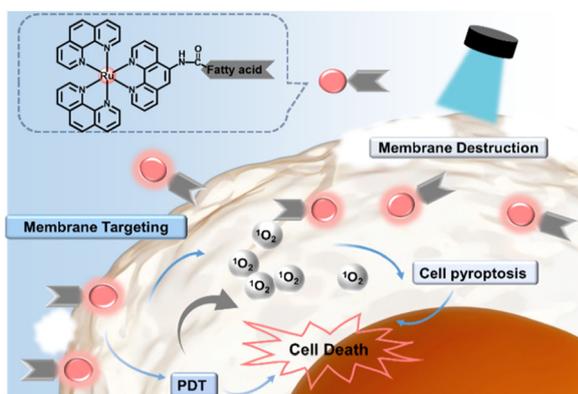
Scheme 1 Schematic representation of anticancer treatment with Ru–Cn.
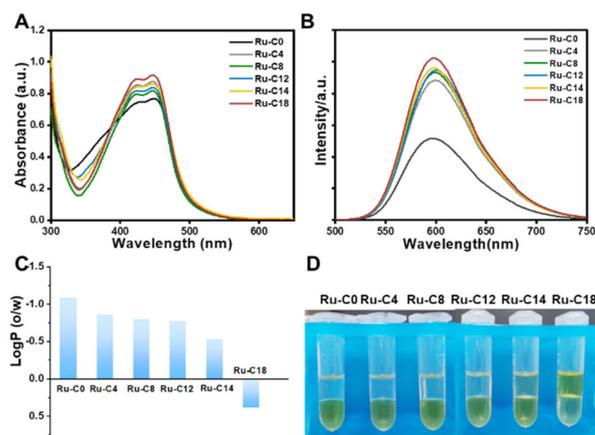
Fig. 1 (A) UV-vis absorption and (B) fluorescence emission spectra of Ru and Ru−Cn complexes (25 μM in PBS with 1% DMSO) recorded at λ = 465 nm. (C) Partition coefficients (log P) of Ru−Cn derivatives in an *n*-octanol/water system. (D) Digital photograph of phase separation between the aqueous and organic layers.

Dalton Transactions

Paper

rescence intensity. This observation can be primarily attributed to the incorporation of fatty acids, which decreases complex solubility and promotes aggregation. In the aggregated state, molecular free rotation is constrained, thereby substantially suppressing non-radiative transitions and improving radiative efficiency. Additionally, aggregation enhances π–π stacking interactions among molecules, thereby further increasing the fluorescence quantum yield. Through precise modulation of the fatty acid chain length and structural architecture, the solubility and aggregation behavior of the complexes can be finely tuned to optimize fluorescence performance. Notably, although the emission wavelength of these complexes remained around 597 nm, the enhancement in fluorescence intensity was not accompanied by a significant spectral shift. These findings indicate that fatty acid modification primarily influences non-radiative transition processes with minimal impact on the distribution of excited-state energy.

The n-octanol/water partition coefficient, commonly employed as a key parameter for assessing drug hydrophobicity, allows for the calculation of concentration distribution between the two phases by measuring the absorbance of test samples in the aqueous phase against standard curves of varying concentrations. The Ru–Cn complexes exhibited partition coefficients of −1.08, −0.85, −0.79, −0.77, −0.53, and 0.39 (Fig. 1C), respectively, reflecting a gradual increase with the elongation of the carbon chain and corresponding enhancement in lipophilicity. Despite their enhanced hydrophobicity, the complexes remained stable in aqueous solutions without precipitation (Fig. 1D), thereby supporting efficient drug transport and cellular uptake. These findings suggest that extending the carbon chain length simultaneously enhances drug lipophilicity and improves dispersibility in solution, consequently promoting increased bioavailability and therapeutic efficacy.

Fluorescence quantum yields were determined using [Ru(bpy)$_3$]$^{2+}$ as a reference standard, resulting in values of 0.45, 0.68, 0.77, 0.76, 0.75, and 0.75 for Ru(II) complexes (Table S1). Time-correlated single-photon counting (TCSPC) analysis of these complexes (Fig. S13) revealed average fluorescence lifetimes (τ) of 441.11 ns, 497.94 ns, 499.52 ns, 505.96 ns, 500.50 ns, and 497.13 ns at specific wavelengths. The molecular polarity of fatty acids exerts a significant influence on the photophysical properties of ruthenium complexes. Elongation of the carbon chain decreases molecular polarity, thereby modulating the excited-state behavior of the complexes. Within the conjugated system, benzene rings facilitate electronic delocalization through π–π stacking interactions, leading to prolonged excited-state lifetimes and enhanced fluorescence efficiency. A synergistic interaction between fatty acids and benzene rings further contributes to the optimization of optical performance. All spectral data are summarized in Table S1.

Confocal microscopy revealed notable differences in the cellular uptake of the Ru(II) complexes. Under identical experimental conditions, significant variations in uptake efficiency were observed among the six Ru(II) complexes during the same incubation period (Fig. 2). In the first two experimental
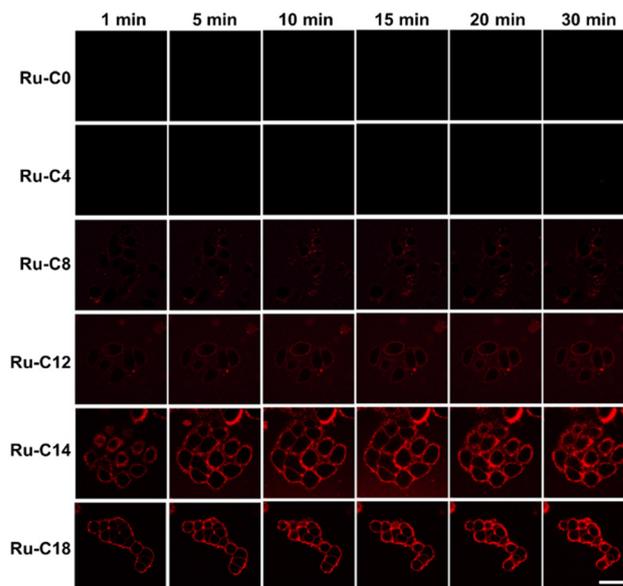

Fig. 2 Cell imaging of Ru–Cn at different time points by confocal imaging (scale bars: 10 μm).

groups, minimal or no red fluorescence signals were detected, indicating a limited capacity for cellular internalization. For Ru-C14 and Ru-C18, red fluorescence exhibited rapid and distinct localization on the cell membrane within 1 minute, suggesting a significantly enhanced uptake efficiency. Flow cytometry further confirmed that cellular internalization increased progressively with increasing carbon chain length under consistent time and concentration conditions (Fig. S14). Moreover, the uptake of the same complex showed a positive correlation with incubation time at equivalent concentrations (Fig. S15). These findings indicate that elongation of the fatty acid carbon chain enhances drug–membrane binding interactions, thereby substantially improving cellular uptake efficiency.

Flow cytometry analysis of cellular drug uptake revealed significant differences in internalization efficiency among the six Ru(II) complexes within the same time frame. Cellular uptake efficiency was markedly reduced at 4 °C compared to that of the control group, underscoring the impact of temperature on cellular metabolic activity. Low temperature reduces membrane fluidity and protein mobility, thereby inhibiting endocytic processes. It also reduces cellular metabolic rates and diminishes energy supply, thereby collectively impairing drug uptake and transport. These factors contribute to the significantly reduced internalization efficiency observed under cold conditions. Unexpectedly, endocytosis inhibitors such as amiloride and the clathrin-mediated inhibitor chlorpromazine (CPZ) did not exert a significant inhibitory effect on cellular drug uptake across various experimental conditions. In contrast, the caveolin-mediated inhibitor methyl-β-cyclodextrin (mβCD) markedly suppressed Ru-C18 internalization, highlighting the predominant involvement of caveolin-dependent pathways (Fig. S16). These findings suggest that the cellular

Published on 28 October 2025. Downloaded on 5/23/2026 7:07:32 PM.

uptake of polypyridyl Ru(II) complexes is not only dependent on energy availability but also involves caveolin-mediated endocytic pathways.

The singlet oxygen generation capacity of Ru–Cn complexes was quantified by monitoring the fading reaction of *N*,*N*-dimethyl-4-nitrosoaniline (RNO) in the presence of L-histidine (Fig. 3). Upon excitation of the photosensitizer at specific wavelengths, molecular oxygen is converted into singlet oxygen ($^1O_2$). The histidine radical formed through the reaction between singlet oxygen and L-histidine consumes RNO in the solution, resulting in a decrease in its concentration. Changes in the UV absorbance of RNO at $\lambda = 440$ nm were monitored to quantify the amount of singlet oxygen produced. A gradual decrease in the absorbance of RNO at 440 nm was observed with increasing illumination time. Using $[Ru(bpy)_3]^{2+}$ as a reference standard ($\Phi(^1O_2) = 0.22$), the singlet oxygen quantum yields of the ruthenium complexes were calculated, yielding values of 0.08, 0.24, 0.23, 0.22, 0.22, and 0.15, as presented in Table S2. Compared to the reference ruthenium compound, these complexes exhibited a significant enhancement in singlet oxygen quantum yield.

Fig. S17 displays the time-dependent absorbance changes of various Ru complexes over a 30-minute period, represented by distinct colored lines. These data indicate that all complexes exhibit a progressive increase in absorbance, suggesting ongoing chemical reactions or molecular interactions that influence their optical properties. Differences in reaction rates are reflected in the varying slopes of the curves. Ru-C12 and Ru-C14 display steeper slopes, indicating more rapid increases

in absorbance, which may be attributed to their distinct structural or electronic features.

The fluorescent probe 2′,7′-dichlorodihydrofluorescein diacetate (DCFH-DA) functions through hydrolysis to generate the non-fluorescent compound dichlorodihydrofluorescein (DCFH), which subsequently accumulates within cells. Upon exposure to photosensitizers or reactive oxygen species (ROS) generators, DCFH undergoes oxidation to form fluorescent 2′,7′-dichlorofluorescein (DCF), which emits green fluorescence and enables quantitative detection of ROS. Under dark conditions, no significant ROS production was observed following drug internalization. Upon exposure to 465 nm light, the Ru(II) complex generated ROS, which oxidized DCFH to fluorescent dichlorofluorescein (DCF). Pronounced green fluorescence was observed in cells treated with Ru-C12, Ru-C14, and Ru-C18 under 465 nm illumination (Fig. S18), indicating significant intracellular ROS generation. Conversely, the Ru, Ru-C4, and Ru-C8 groups exhibited no detectable fluorescence. This absence can likely be attributed to low cellular uptake efficiency under short-term incubation with low drug concentrations. Although Ru-C18 generated slightly lower levels of ROS compared to Ru-C14, its extended fatty acid chain and increased lipophilicity contributed to enhanced membrane penetration.

HeLa and Hep-G2 cells were utilized to evaluate the anticancer efficacy of Ru–Cn (Fig. 4A, and Table S3). Under dark conditions, all ruthenium complexes exhibited minimal cytotoxicity against both HeLa and Hep-G2 cells (IC$_{50}$ > 50 μM). However, a significant time-dependent increase in cytotoxic activity was observed upon visible light irradiation. The cytotoxic effect was notably enhanced with increasing alkyl chain length. Following 0.5 h of irradiation, the IC$_{50}$ values of Ru-C12 to Ru-C18 for both cell lines decreased to sub-micromolar concentrations, ranging from 0.28 to 1.81 μM. Upon complete photoactivation for 2 h, Ru-C14 and Ru-C18, which possess long alkyl chains, demonstrated the highest cytotoxic activity among all tested complexes (Hep-G2: 0.29 ± 0.02 μM; HeLa: 0.28 ± 0.02 μM). Prolonging the irradiation time to 2 hours resulted in a 1.3- to 8.2-fold enhancement in the cytotoxic activity of each complex. Notably, Ru-C18 exhibited the most pronounced increase in cytotoxicity in Hep-G2 cells (IC$_{50}$: 0.51 ± 0.04 μM at 0.5 h *vs.* 0.29 ± 0.02 μM at 2 h).

These results indicate that the alkyl chain structure exerts a significant influence on intracellular ROS production by modulating transmembrane efficiency, thereby enhancing cytotoxicity and demonstrating superior PDT efficacy. In subsequent co-localization experiments, the subcellular distribution of Ru-C18 was examined as a representative model. Lyso-Tracker® Green (LTG) and Mito-Tracker® Green (MTG), which are widely utilized fluorescent probes for labeling lysosomes and mitochondria, were employed. These probes specifically bind to acidic compartments and depend on the mitochondrial membrane potential to achieve accurate organelle localization. As shown in Fig. 4B, following 1 hour of incubation, a clear overlap was observed between the drug's fluorescence signal and that of the lysosomal probe, indicating
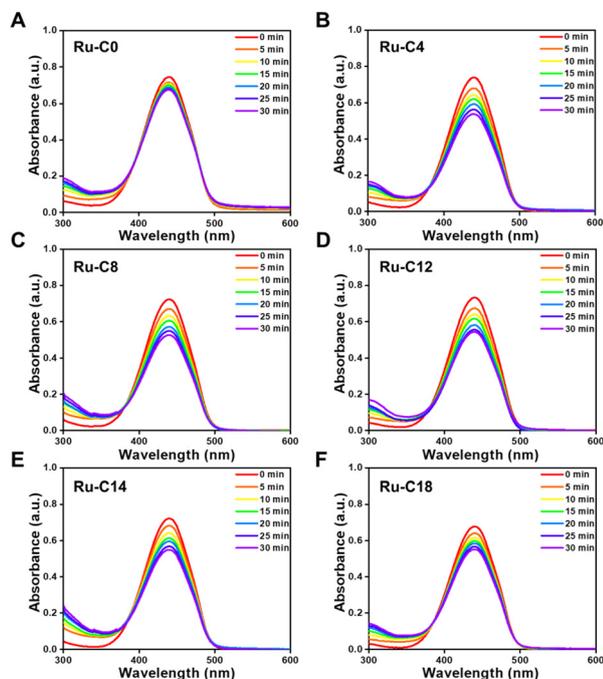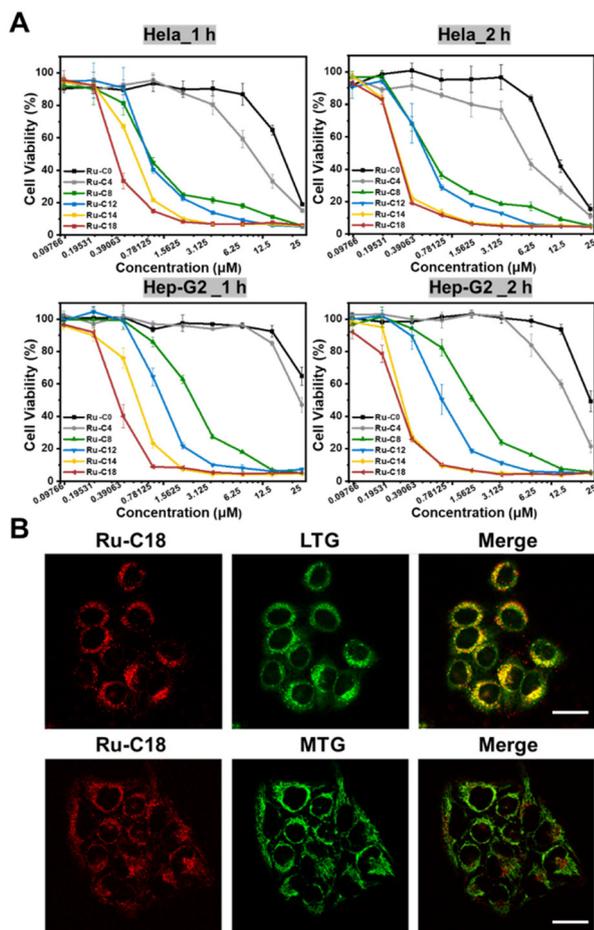

Fig. 3 ROS generation by Ru–Cn (A)–(F) upon irradiation with 465 nm light (10 mW cm^{-2}).
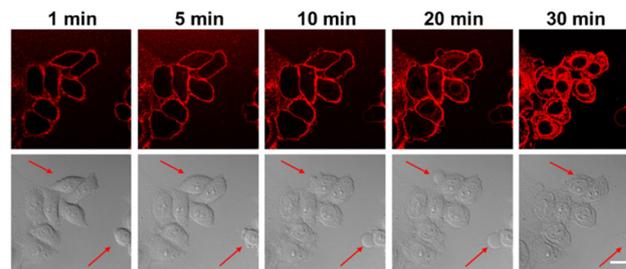
Fig. 4 (A) Cell viability of HeLa and Hep-G2 cells treated with Ru−Cn complexes after different light irradiated times. (B) Confocal microscopy images of cells co-cultured by Ru-18 with Lyso-Tracker® Green and Mito-Tracker® Green probes (scale bars: 50 μm).

Fig. 5 Time-lapse confocal microscopy images showing morphological changes in Hep-G2 cells treated with Ru-C18 under irradiation with 465 nm light (scale bar: 10 μm).

specific accumulation of Ru-C18 within lysosomes. The colocalization coefficient between Ru-C18 and the lysosomal probe was determined to be 0.91, while that with the mitochondrial probe was 0.14, as quantitatively analyzed using ImageJ software.

To more intuitively illustrate the differential therapeutic effects, live/dead cell staining reagents were utilized to evaluate the treatment efficacy of six Ru(II) complexes. Calcein acetoxymethyl ester (calcein-AM) generates green fluorescence in viable cells following intracellular esterase-mediated hydrolysis, whereas propidium iodide (PI) stains cells with compromised membrane integrity, emitting red fluorescence.

Fig. S19 displays widespread green fluorescence in the Ru and Ru-C4 groups, indicating minimal therapeutic effectiveness at comparable concentrations. In contrast, the Ru-C8, Ru-C12, Ru-C14, and Ru-C18 groups exhibit pronounced red fluorescence, which suggests significant membrane disruption and structural degradation. This membrane rupture is consistent with the pyroptotic morphology, as confirmed by confocal microscopy of Hep-G2 cells treated with Ru-C18 (Fig. 5). Under

continuous irradiation at a 2% confocal laser power and a wavelength of 465 nm for 30 minutes, observable changes in the cell morphology were recorded. Following the binding of the drugs to the cell membrane, bubble formation was observed on the membrane surface upon light exposure, leading to progressive cell swelling and eventual rupture, culminating in cell death. These findings suggest that light-induced swelling and pyroptosis represent the primary mechanisms through which Ru complexes exert their cytotoxic effects on cancer cells.

The activation of caspase-1 represents a key biochemical marker of pyroptosis and plays a central role in the canonical inflammasome signaling pathway. To evaluate intracellular caspase-1 activity, a caspase-1 activity assay kit was employed. This assay utilizes the substrate Ac-YVAD-pNA (acetyl-Tyr-Val-Ala-Asp *p*-nitroanilide), which is specifically cleaved by caspase-1 to release the yellow chromogenic product *p*-nitroaniline (pNA). The enzymatic activity of caspase-1 can be quantitatively determined by measuring the absorbance at 405 nm. As illustrated in Fig. S20, upon irradiation at 465 nm, the caspase-1 activity in HepG2 cells treated with Ru-18 was markedly elevated compared to that in the PBS control group, indicating that Ru-18 induces increased caspase-1 activation in response to light exposure. Under dark conditions, the Ru-18 treatment group exhibited negligible levels of caspase-1 activity. These findings highlight the critical role of Ru-18 in promoting caspase-1 activation under specific photonic conditions and confirm that light exposure is essential for the modulation of pyroptotic pathways through the Ru-18 complex. Furthermore, the results demonstrate that Ru-C18 effectively generates $^1O_2$ upon excitation with 465 nm light, thereby inducing pyroptotic cell death in tumor cells.

Conclusions

Through the design of ruthenium(II) complexes functionalized with fatty acids of differing carbon chain lengths, membrane affinity and organelle-targeting specificity are markedly enhanced, leading to improved photosensitizing performance and increased cellular uptake efficiency. This strategy facilitates selective, light-activated cancer cell destruction in PDT.

Among these complexes, Ru-C18 exhibits the highest therapeutic efficacy and demonstrates sub-molar cytotoxicity ($IC_{50} \approx$ 0.3 μM) under irradiation with 465 nm light. Ru-C18 enters cells *via* caveolin-mediated endocytosis and generates abundant ROS upon light irradiation, thereby inducing characteristic pyroptotic morphological features, including membrane blebbing, cellular swelling, and osmotic lysis. Ultimately, it efficiently targets and eradicates cancer cells *via* the gasdermin-mediated pyroptotic pathway. The fatty acid chain modification strategy presented in this study provides a promising avenue for the development of advanced photosensitizers.

Experimental section

Materials and instruments

$RuCl_3 \cdot nH_2O$, *o*-phenanthroline, 1,10-phenanthrolin-5-amine, and NH_4PF_6 were purchased from McLean Biochemical Co., Ltd. Butyric acid (C4), octanoic acid (C8), lauric acid (C12), myristic acid (C14), and stearic acid (C18) were purchased from Aladdin Biochemical Technology Co., Ltd. Calcein-AM/PI, Mito-Tracker Green, Lyso-Tracker Green, fetal calf serum (FCS), and assay kits were purchased from Beyotime Biotechnology Co., Ltd. Hep-G2 and HeLa were obtained from the National Collection of Authenticated Cell Cultures. All solvents and reagents were used without further purification.

The ^1H NMR spectra were acquired using a Bruker AV-500M spectrometer, UV-visible absorption spectra using a Shimadzu UV-2600, fluorescence spectra using a JASCO FP-6500 fluorimeter, and confocal images using a Zeiss LSM 880 confocal microscope. For blue light excitation, a Beijing Princes Technology Co., Ltd PL-LED100F 465 nm-laser served as the light source.

Synthesis of ruthenium complexes

Synthesis of Ru(phen)₂Cl₂. 5 mL of dimethylformamide (DMF) solution with 260 mg of $RuCl_3 \cdot 3H_2O$, 378 mg of *o*-phenanthroline and 424 mg of lithium chloride was refluxed under a N_2 atmosphere at 140 °C for 8 h. After cooling to room temperature, a small amount of acetone was added and then kept at 4 °C for 12 h. The precipitate was collected by centrifugation, washed with water, acetone and ether 2–3 times, respectively, and vacuum dried to obtain the solid product.

Synthesis of Ru(phen)₂(phen-NH₂)Cl₂. 10 mL of ethylene glycol solution with 150 mg of Ru(phen)₂Cl₂ and 97.5 mg of 1,10-phenanthrolin-5-amine was heated to 140 °C and stirred under a N_2 atmosphere for 12 h. Then, the mixture was cooled to room temperature and 10 mL of saturated aqueous NH_4PF_6 solution was added to precipitate the product in the form of phosphate salt. The precipitate was washed with water to obtain the crude product, which was then purified by column chromatography on basic alumina using acetonitrile as the eluent. The product was dissolved in acetone, and an excess amount of tetrabutylammonium chloride was added to precipitate the product as the chlorine salt. After washing with water to remove excess NH_4PF_6, the precipitate was dried and

purified through column chromatography. The obtained product was dissolved in acetone and then a five-fold excess of a saturated solution of tetrabutylammonium chloride acetate tetrabutylammonium hexafluorophosphate in acetone was added. Solid will precipitate out. The solid product was washed with acetone and ether 2–3 times to obtain the product existing in the form of a chloro complex.

Ru(phen)₂Cl₂(phen-NH₂)-fatty acid. The polypyridine Ru(ɪɪ) complex Ru(phen)₂Cl₂ (phen-NH₂)Cl₂ was combined with fatty acids of varying carbon chain lengths. The selected fatty acids included butyric acid (C4), octanoic acid (C8), lauric acid (C12), myristic acid (C14), and stearic acid (C18). The synthetic method is as follows.

Synthesis of Ru(phen)₂Cl₂(phen-NH₂)-C4. In a 25 mL flask, butyric acid (90 μL, 1 mmol) was dissolved in 1 mL of chloroform, followed by the addition of 500 μL of sulfoxide. After stirring at room temperature for 4 h, the chloroform and sulfoxide were removed. Subsequently, Ru(phen)₂(phen-NH₂)Cl₂ (100 mg, 0.15 mmol), triethylamine (40 μL, 0.3 mmol), and 4-dimethylaminopyridine (10 mg, 0.075 mmol) were sequentially added. The reaction mixture was stirred at room temperature in 3 mL anhydrous DMF for 6 h, followed by a 12 h reaction at 45 °C. The solvent DMF was removed by using 5 mL of dichloromethane and 20 to 25 mL of *n*-hexane. The resulting solid was precipitated by adding 5 mL of ether. The product was purified by column chromatography, followed by drying to yield the final product.

Synthesis of Ru(phen)₂Cl₂(phen-NH₂)-C8. Using the same synthesis method, butyric acid was replaced with octanoic acid.

Synthesis of Ru(phen)₂Cl₂(phen-NH₂)-C12. Using the same synthesis method, butyric acid was replaced by lauric acid.

Synthesis of Ru(phen)₂Cl₂(phen-NH₂)-C14. Using the same synthesis method, butyric acid was replaced with myristic acid.

Synthesis of Ru(phen)₂Cl₂(phen-NH₂)-C18. Using the same synthesis method, butyrate was replaced with stearic acid.

Ru(phen)₂Cl₂(phen-NH₂)Cl₂. Yield: 55%. ESI-MS[CH_3OH, m/z]: 328.56 ($C_{36}H_{25}N_7Ru$ [M − 2Cl]$^{2+}$, found: 328.56. ^1H NMR (500 Hz, DMSO-*d6*) δ 8.96 (d, J = 8.5 Hz, 1H), 8.77 (dd, J = 15.4, 6.9 Hz, 4H), 8.39 (s, 4H), 8.29 (d, J = 9.3 Hz, 1H), 8.12–8.04 (m, 4H), 8.01 (d, J = 4.5 Hz, 1H), 7.79 (dd, J = 24.5, 16.2 Hz, 4H), 7.72–7.67 (m, 1H), 7.56 (d, J = 6.0 Hz, 1H), 7.49–7.44 (m, 1H), 7.10 (s, 1H), 7.01 (s, 2H).

Ru(phen)₂Cl₂(phen-NH₂)-C4. Yield: 62%. ESI-MS[CH_3OH, m/z]: 363.58 ($C_{40}H_{31}N_7ORu$ [M − 2Cl]$^{2+}$, found: 363.58. ^1H NMR (500 Hz, DMSO-*d6*) δ 10.81 (s, 1H), 9.07 (d, J = 7.1 Hz, 1H), 8.84–8.62 (m, 6H), 8.40 (s, 4H), 8.23 (s, 1H), 8.09 (d, JJ = 7.7 Hz, 4H), 7.74 (d, J = 29.8 Hz, 6H), 6.99 (d, J = 7.9 Hz, 1H), 2.63 (s, 2H), 1.78–1.67 (m, 2H), 1.00 (t, J = 7.7 Hz, 3H).

Ru(phen)₂Cl₂(phen-NH₂)-C8. Yield: 65%. ESI-MS[CH_3OH, m/z]: 391.61 ($C_{44}H_{39}N_7ORu$ [M − 2Cl]$^{2+}$, found: 391.61. ^1H NMR (500 Hz, DMSO-*d6*) δ 10.79 (s, 1H), 9.06 (d, J = 7.4 Hz, 1H), 8.84–8.60 (m, 6H), 8.39 (s, 4H), 8.21 (s, 1H), 8.12–8.03 (m, 4H), 7.84–7.64 (m, 6H), 6.98 (d, J = 5.5 Hz, 1H), 2.64 (t, J = 7.1 Hz, 2H), 1.69 (s, 2H), 1.31 (d, J = 29.0 Hz, 8H), 0.86 (t, J = 4.3 Hz, 3H).

Ru(phen)₂Cl₂(phen-NH₂)-C12. Yield: 60%. ESI-MS[CH_3OH, m/z]: 419.65 ($C_{48}H_{47}N_7ORu$ [M − 2Cl]$^{2+}$, found: 419.65. ^1H

NMR (500 Hz, DMSO-*d6*) δ 10.84 (s, 1H), 9.08 (d, J = 7.7 Hz, 1H), 8.85–8.62 (m, 6H), 8.41 (s, 4H), 8.22 (s, 1H), 8.09 (d, J = 2.3 Hz, 4H), 7.79 (s, 6H), 6.99 (d, J = 6.8 Hz, 1H), 2.66 (d, J = 7.2 Hz, 2H), 1.69 (s, 2H), 1.21 (d, J = 10.7 Hz, 16H), 0.83 (d, J = 3.6 Hz, 3H).

Ru(phen)$_2$Cl$_2$(phen-NH$_2$)-C14. Yield: 67%. ESI-MS[CH$_3$OH, m/z]: 433.66 (C$_{50}$H$_{51}$N$_7$ORu [M − 2Cl]$^{2+}$, found: 433.66.^{1}H NMR (500 Hz, DMSO-*d6*) δ 10.79 (s, 1H), 9.06 (d, J = 8.6 Hz, 1H), 8.81–8.65 (m, 6H), 8.40 (d, J = 3.9 Hz, 4H), 8.22 (dd, J = 7.3, 5.7 Hz, 1H), 8.08 (ddd, J = 14.2, 10.0, 4.7 Hz, 4H), 7.81–7.68 (m, 6H), 6.99 (d, J = 7.6 Hz, 1H), 2.65 (t, J = 7.3 Hz, 2H), 1.69 (dt, J = 14.9, 7.4 Hz, 2H), 1.42–1.16 (m, 20H), 0.83 (t, J = 7.0 Hz, 3H).

Ru(phen)$_2$Cl$_2$(phen-NH$_2$)-C18. Yield: 62%. ESI-MS[CH$_3$OH, m/z]: 460.03 (C$_{54}$H$_{59}$N$_7$ORu [M − 2Cl]$^{2+}$, found: 460.03. ^{1}H NMR (500 Hz, DMSO-*d6*) δ 10.80 (s, 1H), 9.07 (d, J = 8.6 Hz, 1H), 8.78 (d, J = 4.6 Hz, 4H), 8.72 (d, J = 8.4 Hz, 1H), 8.66 (s, 1H), 8.40 (d, J = 4.4 Hz, 4H), 8.22 (s, 1H), 8.11–8.07 (m, 4H), 7.82–7.74 (m, 6H), 6.99 (d, J = 7.6 Hz, 1H), 2.65 (t, J = 7.3 Hz, 2H), 1.71–1.65 (m, 2H), 1.42–1.12 (m, 28H), 0.84 (t, J = 7.0 Hz, 3H).

Quantum yields of singlet oxygen ($^1O_2$) and fluorescence lifetime

The tested Ru samples were added to the PBS solution containing L-histidine (10 mM) and RNO (20 μM) to achieve a drug absorbance of A465 nm = 0.1. The solution was then irradiated with 465 nm light (10 mW cm^{-2}) and the absorbance of RNO at 440 nm was recorded every 5 minutes after each light exposure. The changes in absorbance at different time points were plotted to obtain a curve, with time on the x-axis and $A_0 − A$ (A_0 representing the absorbance without light exposure) on the y-axis. A linear fitting curve was then created. The calculation for singlet oxygen quantum yield is as follows, with Ru(bpy)$_3$Cl$_2$ (Φ_{ref} = 0.22) serving as the reference group. The fluorescence quantum yield was calculated with [Ru(bpy)$_3$]$^{2+}$ as the reference standard using the following formula:

$$\Phi_{sample} = \frac{\Phi_{ref} \times S_{sample} \times I_{ref}}{S_{ref} \times I_{sample}}$$

$$I = I_0 \times (1 - 10^{-A_\lambda})$$

where S_{sample} is the slope of the sample linear equation; S_{ref} is the slope of the control; I is the absorption correction factor; I_0 is the intensity of the light source during irradiation; and A_λ is the absorbance at 465 nm in the absence of light exposure.

Under room temperature conditions, fluorescence lifetime detection was conducted using Time-Correlated Single Photon Counting (TCSPC) spectroscopy. At a specific concentration, an excitation wavelength of 465 nm and an emission wavelength of 600 nm were set with a time range of 10 μs. The decay curve of fluorescence intensity under specific wavelengths was obtained. The fluorescence lifetime of the complex was calculated by fitting, weighting and using the formula.

$$R(t) = B_1 e^{(-t/\tau 1)} + B_2 e^{(-t/\tau 2)} + B_3 e^{(-t/\tau 3)} + B_4 e^{(-t/\tau 4)}$$

where R is the total fluorescence intensity; B_1, B_2, B_3 and B_4 are constants; and τ is the fluorescence lifetime.

Intracellular ROS detection

The cellular ROS production was assessed based on the fluorescence intensity of the reactive oxygen species probe DCFH-DA.[47] Hep-G2 cells were seeded in a 48-well plate at a density of 1×10^4 cells per well. The plate was then placed in a cell culture incubator at 37 °C, with 5% CO$_2$ and saturated humidity for 24 hours in medium containing 10% fetal bovine serum. After incubating the cells with 1 μM Ru, Ru-C4, Ru-C8, Ru-C12, Ru-C14, and Ru-C18 for 1 hour, the drugs were removed, and the cells were exposed to 465 nm light (10 mW cm^{-2}) for 30 minutes. Then, the culture medium was removed, and 20 μM DCFH-DA probe was added. After a 20-minute incubation, the probe was removed, and the cells were observed under a fluorescence microscope.

log $P_{o/w}$ measurement

Specifically, 0.5 mL of octanol, 0.45 mL of water, and 50 μL of 1 mM aqueous solution of poly-pyridine Ru(II) complex were mixed uniformly in a shaking tank. After 24 hours, a portion of the aqueous phase was taken and measured with a UV spectrophotometer. Standard curves were established using UV absorbance values corresponding to different gradient drug concentrations. The distribution patterns of the drug in both water and octanol were then calculated based on these standard curves and the absorbance measurements from the test aqueous phase.

$$\log K_{o/w} = \log A_{octanol}/A_{water}$$

where $K_{o/w}$ is the octanol/water partition coefficient; $A_{octanol}$ represents the absorbance of the sample being tested in the octanol phase; and A_{water} represents the absorbance of the sample being tested in the aqueous phase.

Cell culture

After washing the cells twice with 2 mL PBS buffer, 1 mL of trypsin was added and digested in a culture incubator. Depending on the adhesive properties of different cell types, it was ensured that the trypsin digestion time was not too long. Once most cells appear rounded under microscopic observation, the trypsin was quickly removed and 2 mL of serum-containing medium was added. The cells were then gently dispersed into a sterile centrifuge tube, and centrifuged at 1000 rpm for 3 minutes to discard the supernatant. The cells were resuspend by adding appropriate amounts of medium. Finally, the required cell suspension was transferred to 25 cm^2 culture flasks and placed back into the incubator for further cultivation or use in various experiments.

Cellular uptake determined using a flow cytometer

Hep-G2 cells were seeded in a 6-well plate at a density of 1×10^6 cells per well and cultured in an incubator for 24 hours. The cells were then incubated with different Ru complexes

(Ru, Ru-C4, Ru-C8, Ru-C12, Ru-C14, and Ru-C18) at 25 μM with varying incubation times (0.5, 1, 2, 4, and 8 hours, respectively). After the incubation, the culture medium was removed, and the cells were washed 2–3 times with PBS and HBSS. The cells were collected by trypsinase digestion and assessed for drug uptake efficiency using a flow cytometer (BD FACS Calibur).

Under similar culture conditions, different endocytosis inhibitors, including chlorpromazine (CPZ, 20 μg mL^{-1}), amiloride (AMI, 2 mM), and methyl-β-cyclodextrin (m-β-CD, 5 mM), were used to pretreat the cells for 30 minutes. After pretreatment, Ru-C18 (25 μM) was added and the cells were incubated at 37 °C for 4 hours. One group of cells was incubated at 4 °C for 4 hours, while the control cells underwent no treatment. After the incubation, the culture medium was removed, and the cells were washed 2–3 times with PBS and HBSS, collected by trypsinase digestion, and assessed for drug uptake efficiency using a flow cytometer (BD FACS Calibur) to determine the uptake pathway under different inhibition conditions.

Cytotoxicity testing

The MTT method detects cell viability by measuring the activity of succinate dehydrogenase in the mitochondria of living cells. Thiazolyl blue (MTT) is reduced to by the enzyme to an insoluble, bluish-purple crystal (absent in dead cells). After dissolving the crystals in DMSO, the cytotoxicity of the drug is analyzed by measuring the absorbance at 490 nm using a microplate reader.

Hep-G2 and HeLa cells were separately seeded at 6×10^3 cells per well in a 96-well plate with a volume of 100 μL per well. The outer wells received the same volume of sterile PBS. The cells were incubated in a 37 °C, 5% CO$_2$ incubator for 24 hours. Different drug concentrations were added using a two-fold dilution method, with 3 to 5 parallel groups for each concentration. The cells were then incubated for 0.5 h, 1 h, and 2 h, followed by dark treatment or exposure to a 465 nm light source (10 mW cm^{-2}, 30 minutes). After overnight incubation, MTT (25 μL per well, 5 mg mL^{-1}) was added and incubated for 2 to 4 hours. The medium was then removed, and 150 μL of DMSO was added to each well for dissolution. After shaking, the absorbance at 490 nm for each well was measured. The IC$_{50}$ value was calculated using GraphPad Prism software.

$$\text{Cell viability} = \frac{\text{OD}_{\text{drug}} - \text{OD}_{\text{blank}}}{\text{OD}_{\text{control}} - \text{OD}_{\text{blank}}} \times 100\%$$

Laser confocal cell experiments

The Hep-G2 cells were appropriately seeded in laser confocal culture dishes. After adherent growth, a 25 μM complex was added and incubated for 1 hour. Subsequently, the drug was removed, fresh medium was added, and cultivation was continued. Lyso-Tracker Green (5 μM, 2 hours) and Mito-Tracker Green (150 nM, 30 minutes) were introduced for staining. Upon completion of staining, the cells were washed 2–3 times with serum-free medium and PBS. Cellular observations were then conducted under a Zeiss LSM 880 confocal microscope with a 63× oil lens.

Live/dead cell staining assay

Fluorescence intensity was utilized to assess the distribution of cell death using the calcein-AM/PI dual staining reagents. Approximately 2×10^4 Hep-G2 cells were seeded in a 48-well plate. After 24 hours of adherent growth, 1 μM complex was added and incubated for 1 hour. Following drug removal, light exposure was conducted using a 465 nm light source (10 mW cm^{-2}, 30 min). The cells were then placed in an incubator for 24 hours. Subsequently, AM (4 μM) and PI (6 μM) were added for staining, incubated for 15 minutes, and examined under a fluorescence microscope.

Conflicts of interest

The authors declare that they do not have any commercial or associative interest that represents a conflict of interest in connection with the work submitted.

Data availability

All data collected during the study are included in the article and its supplementary information (SI), with no additional data provided. Supplementary information is available. The supplementary information includes comprehensive experimental data, such as structural characterization (1H NMR, ESI-MS), fluorescence lifetime decay curves, flow cytometry analysis, ROS generation profiles, microscopic visualization of live and dead cells, and specific Caspase-1 activation assays. See DOI: https://doi.org/10.1039/d5dt02102b.

Acknowledgements

References

1 R. L. Siegel, T. B. Kratzer, A. N. Giaquinto, H. Sung and A. Jemal, *CA-Cancer J. Clin.*, 2025, **75**, 10–45.
2 F. Bray, M. Laversanne, H. Sung, J. Ferlay, R. L. Siegel, I. Soerjomataram and A. Jemal, *CA-Cancer J. Clin.*, 2024, **74**, 229–263.
3 Y. Yang, L. Liu, Y. Tian, M. Gu, Y. Wang, M. Ashrafizadeh, A. R. Aref, I. Cañadas, D. J. Klionsky, A. Goel, R. J. Reiter,

Y. Wang, M. Tambuwala and J. Zou, *Cancer Lett.*, 2024, **587**, 216659.

4 L. Tang, Y. Yin, Y. Cao, H. Liu, G. Qing, C. Fu, Z. Li, Y. Zhu, W. Shu, S. He, J. Gao, Y. Zhang, Z. Wang, J. Bu, X. Li, M. Zhu, X. Liang and W. Wang, *ACS Nano*, 2024, **18**, 32103–32117.

5 E. Armstrong-Gordon, D. Gnjidic, A. J. McLachlan, B. Hosseini, A. Grant, P. J. Beale and N. J. Wheate, *J. Cancer Res. Clin. Oncol.*, 2018, **144**, 1561–1568.

6 J. Graham, M. Muhsin and P. Kirkpatrick, *Nat. Rev. Drug Discovery*, 2004, **3**, 11–12.

7 P. D. O'Dowd, D. F. Sutcliffe and D. M. Griffith, *Coord. Chem. Rev.*, 2023, **497**, 215439.

8 D. Spector, A. Zharova, V. Bykusov, G. Karetnikov, E. Beloglazkina and O. Krasnovskaya, *Coord. Chem. Rev.*, 2025, **541**, 216808.

9 S. Rottenberg, C. Disler and P. Perego, *Nat. Rev. Cancer*, 2021, **21**, 37–50.

10 M. Li, S. Zhou, Y. Zhang, J. Li and K. Zhang, *Nanomaterials*, 2025, **15**, 1262.

11 S. Son, J. Kim, J. Kim, B. Kim, J. Lee, Y. Kim, M. Li, H. Kang and J. S. Kim, *Chem. Soc. Rev.*, 2022, **51**, 8201–8215.

12 L. Ma, L. Li and G. Zhu, *Inorg. Chem. Front.*, 2022, **9**, 2424–2453.

13 L. Schapira and C. M. Duffy, *CA-Cancer J. Clin.*, 2025, **75**, 277–279.

14 B. Wu, Y. Cheng, L. Li, Z. Du, Q. Liu, X. Tan, X. Li, G. Zhao and E. Li, *Drug Resistance Updates*, 2025, **81**, 101238.

15 L. Wang, X. Zhao, J. Fu, W. Xu and J. Yuan, *Front. Mol. Biosci.*, 2021, **8**, 691795.

16 X. Sun, X. Xu, F. Li, H. Wang, Y. Sun, H. Yang, X. Li, B. Kong, H. Hou, H. Liu and J. Li, *Adv. Funct. Mater.*, 2025, **35**, 2502646.

17 U. Das, U. Basu and P. Paira, *Dalton Trans.*, 2024, **53**, 15113–15157.

18 A. Bergamo and G. Sava, *Dalton Trans.*, 2011, **40**, 7817–7823.

19 M. Sojka and P. Gamez, *Coord. Chem. Rev.*, 2025, **543**, 216902.

20 X. Zeng, Y. Wang, J. Han, W. Sun, H. J. Butt, X. J. Liang and S. Wu, *Adv. Mater.*, 2020, **32**, 2004766.

21 A. Rilak Simović, R. Masnikosa, I. Bratsos and E. Alessio, *Coord. Chem. Rev.*, 2019, **398**, 113011.

22 L. Zeng, P. Gupta, Y. Chen, L. Ji, H. Chao and Z. Chen, *Chem. Soc. Rev.*, 2017, **46**, 5771.

23 M. Bashir, I. A. Mantoo, F. Arjmand, S. Tabassum and I. Yousuf, *Coord. Chem. Rev.*, 2023, **487**, 215169.

24 J. Liu, H. Lai, Z. Xiong, B. Chen and T. Chen, *Chem. Commun.*, 2019, **55**, 994–9914.

25 C. E. Elgar, N. A. Yusoh, P. R. Tiley, N. Kolozsvári, L. G. Bennett, A. Gamble, E. V. Péan, M. L. Davies, C. J. Staples, H. Ahmad and M. R. Gill, *J. Am. Chem. Soc.*, 2023, **145**, 1236–1246.

26 Y. Wang, Y. Hu, H. Zhang, Y. Chen, H. Shi, J. Liu and Q. Zhang, *Dalton Trans.*, 2023, **52**, 8051–8057.

27 J. Zheng, X. Wang, H. Du, R. Zhang, X. Huo, T. Zhou, G. Zhang, F. Wang, Q. Zhou and Z. Zhang, *J. Inorg. Biochem.*, 2025, **262**, 112771.

28 H. Shi, R. C. Marchi and P. J. Sadler, *Angew. Chem., Int. Ed.*, 2025, **64**, e202423335.

29 S. A. McFarland, A. Mandel, R. Dumoulin-White and G. Gasser, *Curr. Opin. Chem. Biol.*, 2020, **56**, 23–27.

30 S. Monro, K. L. Colón, H. Yin, J. Roque, P. Konda, S. Gujar, R. P. Thummel, L. Lilge, C. G. Cameron and S. A. McFarland, *Chem. Rev.*, 2019, **119**, 797–828.

31 Z. Ma, M. He, Z. Zhang, X. Zeng, S. Wang, C. Peng, J. Du, J. Fan, X. Peng and W. Sun, *Adv. Mater.*, 2025, e8713.

32 K. Peng, Y. Zheng, W. Xia and Z. Mao, *Chem. Soc. Rev.*, 2023, **52**, 279–2832.

33 J. Zhang, D. Jiao, X. Qi, Y. Zhang, X. Liu, T. Pan, H. Gao, Z. Liu, D. Ding and G. Feng, *Adv. Sci.*, 2025, **12**, 2410405.

34 X. Su, W. J. Wang, Q. Cao, H. Zhang, B. Liu, Y. Ling, X. Zhou and Z. W. Mao, *Angew. Chem., Int. Ed.*, 2022, **61**, e202115800.

35 Y. Bai, Y. Pan and X. Liu, *Nat. Rev. Mol. Cell Biol.*, 2025, **26**, 501–521.

36 Y. Zheng, K. Peng, Q. Cao and Z. W. Mao, *Angew. Chem., Int. Ed.*, 2025, **64**, e202507186.

37 Y. Zhi, T. Chen, B. Liang, S. Jiang, D. Yao, Z. He, C. Li, L. He and Z. Pan, *J. Inorg. Biochem.*, 2024, **260**, 112695.

38 T. Ma, L. Liu, Y. Zeng, K. Ding, H. Zhang, W. Liu, Q. Cao, W. Xia, X. Xiong, C. Wu and Z. Mao, *Chem. Sci.*, 2024, **15**, 9756–9774.

39 X. Su, B. Liu, W. J. Wang, K. Peng, B. B. Liang, Y. Zheng, Q. Cao and Z. W. Mao, *Angew. Chem., Int. Ed.*, 2023, **62**, e202216917.

40 L. Zhu, J. Hu, X. Wu, J. Zhang, X. Xu, X. Huang, B. Tian, C. Zhao, Y. Du and L. Wu, *Nat. Commun.*, 2025, **16**, 3017.

41 X. Xu, J. Zheng, N. Liang, X. Zhang, S. Shabiti, Z. Wang, S. Yu, Z. Pan, W. Li and L. Cai, *ACS Nano*, 2024, **18**, 9413–9430.

42 B. Liang, S. Jiang, Y. Zhi, Z. Pan, X. Su, Q. Gong, Z. He, D. Yao, L. He and C. Li, *Inorg. Chem. Front.*, 2025, **12**, 2294–2302.

43 A. B. McCullough, J. Chen, N. P. Valentine, T. M. Franklin, A. P. Cantrell, V. M. Darnell, Q. Qureshi, K. Hanson, S. M. Shell and D. L. Ashford, *Dalton Trans.*, 2022, **51**, 10186–10197.

44 M. Jóźwiak, A. Filipowska, F. Fiorino and M. Struga, *Eur. J. Pharmacol.*, 2020, **871**, 172937.

45 C. Park, N. Baek, R. Loebenberg and B. Lee, *J. Controlled Release*, 2020, **324**, 55–68.

46 M. Hou, Q. Yu, L. Yang, H. Zhao, P. Jiang, L. Qin and Q. Zhang, *Front. Oncol.*, 2024, **14**, 1451045.

47 J. Fan, T. Hito and T. W. Chung, *Mol. Cell. Biol.*, 2011, **31**(24), 4938–4950.